Matter

Article

Lattice distortion boosted exceptional electromagnetic wave absorption in high-entropy diborides

Graphical abstract

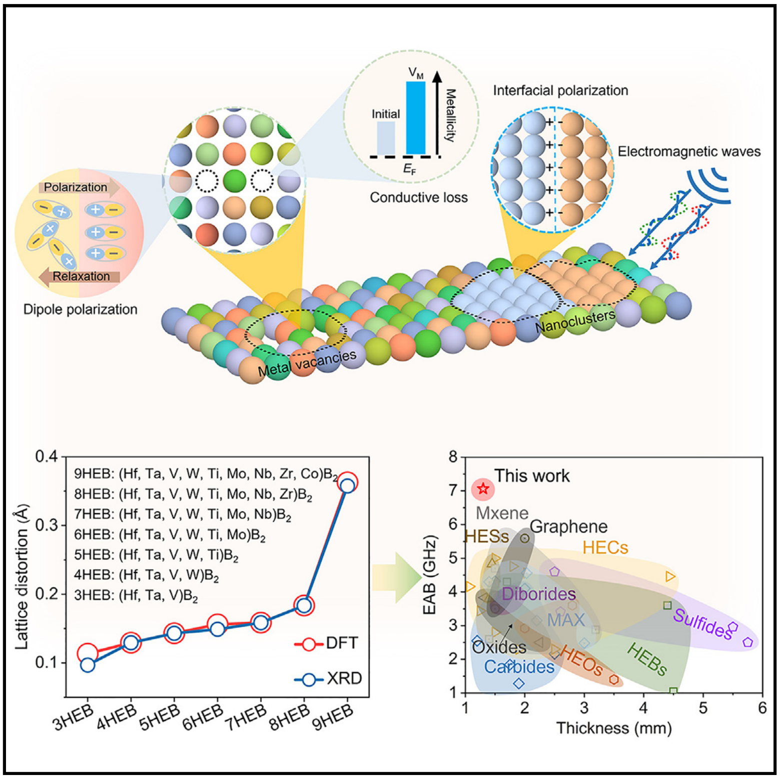

Highlights

- HEBs with good microwave absorption are explored by lattice distortion engineering
- Lattice distortion-caused vacancies boost conduction and dipole polarization losses
- Lattice distortion-caused nanoclusters promote interfacial polarization loss

6 **Development**
Practical, real world, technological considerations and constraints

Authors

Fangchao Gu, Wu Wang, Hong Meng, Yiwen Liu, Lei Zhuang, Hulei Yu, Yanhui Chu

Correspondence

lzhuang@scut.edu.cn (L.Z.),
chuyh@scut.edu.cn (Y.C.)

In brief

Developing high-performance electromagnetic wave absorbents is crucial for addressing the growing global issue of electromagnetic pollution. Here, we employ a lattice distortion engineering strategy to achieve exceptional electromagnetic wave absorption performance in high-entropy diborides, which is primarily attributed to three key mechanisms involving metal vacancy-induced dipole polarization loss and conduction loss as well as nanocluster-induced interfacial polarization loss. This work presents a straightforward approach to significantly enhance the electromagnetic wave absorption performance of ceramic absorbents.

Gu et al., 2025, Matter *8*, 102004
March 5, 2025
https://doi.org/10.1016/j.matt.2025.102004

CellPress

Please cite this article in press as: Gu et al., Lattice distortion boosted exceptional electromagnetic wave absorption in high-entropy diborides, Matter (2025), https://doi.org/10.1016/j.matt.2025.102004

Matter

CellPress

Article

Lattice distortion boosted exceptional electromagnetic wave absorption in high-entropy diborides

Fangchao Gu,[1,4] Wu Wang,[2,3,4] Hong Meng,[1,4] Yiwen Liu,[1] Lei Zhuang,[1,*] Hulei Yu,[1] and Yanhui Chu[1,5,*]

[1]School of Materials Science and Engineering, South China University of Technology, Guangzhou 510641, China
[2]College of Integrated Circuits and Optoelectronic Chips, Shenzhen Technology University, Shenzhen 518118, China
[3]Shenzhen Key Laboratory of Thermoelectric Materials, Department of Physics, Southern University of Science and Technology, Shenzhen 518055, China
[4]These authors contributed equally
[5]Lead contact
*Correspondence: lzhuang@scut.edu.cn (L.Z.), chuyh@scut.edu.cn (Y.C.)
https://doi.org/10.1016/j.matt.2025.102004

PROGRESS AND POTENTIAL With the rapid advancement of wireless communication, electromagnetic pollution has become a significant global concern. Exploring high-performance electromagnetic wave absorbents is an effective way to tackle this problem. Here, we achieve significantly improved electromagnetic wave absorption performance in high-entropy diborides by engineering their lattice distortion. We further identify three key absorption mechanisms responsible for this exceptional electromagnetic wave performance, involving metal vacancy-induced dipole polarization loss and conduction loss as well as nanocluster-induced interfacial polarization loss. The developed high-entropy diboride absorbents show considerable potential for the electromagnetic wave absorption application.

SUMMARY

Electromagnetic pollution has emerged as a severe global issue due to the widespread use of wireless communication, which strongly requires high-performance electromagnetic wave absorbents. Here, we realize exceptional electromagnetic wave absorption performance with an effective absorption bandwidth of 7.2 GHz at an ultralow thickness of 1.5 mm in high-entropy diborides through a lattice distortion engineering strategy. Particularly, we rationally tailor the lattice distortion of high-entropy diborides by manipulating constituent metal elements, and the resultant metal vacancies and chemical nanoclusters are verified to result in enriched electromagnetic wave absorption mechanisms, including (1) metal vacancy-induced dipole polarization loss, (2) metal vacancy-induced conduction loss, and (3) chemical nanocluster-induced interfacial polarization loss. Our work provides a simple and universal approach for effectively enhancing the electromagnetic wave absorption performance of ceramic absorbents.

INTRODUCTION

Popularization of advanced electronic devices and cutting-edge wireless communication technologies have greatly improved social functionality and convenience in daily life. However, the issue of electromagnetic radiation pollution not only disrupts the function of nearby electronic equipment and compromises information security and communication quality but also poses risks to human health.[1,2] The most effective way to address this problem is to develop advanced electromagnetic wave absorbents with features of light weight, strong absorption, thin thickness, and wide absorption bandwidth. To this end, two essential characteristics must be taken into account: impedance matching and dissipation ability.[3–5] Impedance matching refers to the requirement that the impedance of an absorbent should be comparable to that of air to minimize the reflection of electromagnetic waves, whereas such kinds of materials are often wave transparent with limited energy loss. Conversely, improving the dissipation capability of materials commonly reduces impedance matching.[3] This trade-off leads to a great challenge for achieving exceptional electromagnetic wave absorption performance in absorbents.

To resolve this tangled issue, structural design for absorbents is critical, which can span three scales: microscale, nanoscale, and atomic scale. Thus far, there has been extensive research on structural design on the microscale and nanoscale. For

Please cite this article in press as: Gu et al., Lattice distortion boosted exceptional electromagnetic wave absorption in high-entropy diborides, Matter (2025), https://doi.org/10.1016/j.matt.2025.102004

instance, micro-sized graphene-[6,7] or MXene-based dielectric skeletons[8–10] are often coupled with magnetic and/or dielectric components to construct heterogeneous interfaces, giving rise to significant attenuation of microwave energy through conduction loss, polarization loss, and magnetic loss. Additionally, nanoscale core-shell structures, where magnetic components serve as the core and dielectric components as the shell, are also reported.[11–13] The moderate impedance matching between the core and shell components as well as the dielectric and magnetic dissipation mechanisms contribute to improvements in electromagnetic wave absorption properties. Despite progress that has been made, until now, there is limited work on structural design for absorbents at the atomic scale, hindering the exploration of high-performance absorbents with new attenuation mechanisms. Recently, the high-entropy concept involving four core effects—high entropy effect, lattice distortion effect, sluggish diffusion effect, and cocktail effect—has emerged as a promising strategy to tailor the structure of ceramics at the atomic scale.[14–18] These unique features make them highly attractive for a broad range of structural applications, such as high-speed cutting, thermal and environmental protection in hypersonic vehicles, and functional applications such as thermoelectrics, batteries, and catalysts.[19–25] Notably, some preliminary work has also shown the potential of high-entropy ceramics as high-performance single-phase absorbents due to their vast compositional space. For example, (Ti, Zr, Hf, Nb, Ta)C high-entropy carbides (HECs) have been shown to possess improved electromagnetic wave absorption performance compared to their individual components TiC, ZrC, HfC, NbC, and TaC.[26] Similar findings were also reported in the (Ti, Nb, Ta)$_2$FeC MAX phases[27] and (Ca, Sr, Ba, La, Pb)TiO$_3$ high-entropy oxides (HEOs).[28] However, manipulating the structure of single-phase high-entropy ceramics at the atomic scale to achieve remarkable electromagnetic wave absorption performance remains challenging.

In this work, we employ a lattice distortion engineering strategy to realize exceptional electromagnetic wave absorption performance in single-phase high-entropy ceramics through three dielectric loss mechanisms. Specifically, we choose high-entropy diborides (HEBs) as the representative owing to their high intrinsic conductivity (σ) for potentially favorable dielectric loss. Then, we tailor their lattice distortion by gradually introducing constituent metal elements to synthesize 3- to 9-cation HEB (3–9HEB) samples via a simple and universal ultrafast high-temperature synthesis (UHTS) technique that enables the rapid and efficient synthesis of single-phase HEBs in tens of seconds. Lattice distortion has been shown to induce pronounced chemical fluctuations, forming numerous "nanoclusters" to facilitate effective interfacial polarization loss. Lattice distortion has also contributed to the generation of metal vacancies, leading to significant conduction loss and dipole polarization loss. As a result, the 9HEB samples with the greatest lattice distortion can realize an effective absorption bandwidth (EAB, with the reflection loss [RL] less than -10 dB) value of up to 7.2 GHz at an ultra-low thickness of 1.5 mm, outperforming previously reported single-phase electromagnetic wave absorption materials. This study opens a new path to improve the electromagnetic wave absorption performance of ceramic materials.

RESULTS

Tailoring lattice distortion in HEBs

We first predicted lattice distortion of 3–9HEBs through density functional theory (DFT) calculations.[29] The 3HEB starts with Hf, Ta, and V elements, and the compositions of 4–9HEBs are designed to expand by progressively adding W, Ti, Zr, Nb, Mo, and Co elements. As illustrated in Figure 1A, the additional metal elements are expected to give rise to a significant increase in lattice distortion from 0.11 to 0.36 Å for 3–9HEBs, which also indicates the potential to fine-tune lattice distortion in HEBs by regulating their compositions. It is worth noting that there is a leap between the 8HEB (0.18 Å) and 9HEB (0.36 Å), which should be attributed to the dramatic difference in atomic radii between Co (1.25 Å) and the other elements (an average of 1.46 Å) in groups IIIB, IVB, and VB. Subsequently, the as-designed 3–9HEBs were synthesized via the UHTS technique. Based on their X-ray diffraction (XRD) patterns in Figure 1B, corresponding Rietveld refinements with low fitting parameters (R_{wp} and R_p) (Figure S1) and well-refined unit cell parameters with the average values from individual diborides (Table S1), the as-synthesized 3–9HEB samples are confirmed to be single-phase solid solutions, having hexagonal structures with a space group of $P6/mmm$. This crystalline structure can be further confirmed by the interplanar spacing calculated from scanning transmission electron microscopy (STEM) imaging (Figure S2). In addition, as shown in Figure 1A, the lattice distortion of 3–9HEBs evaluated from XRD is also in good alignment with that from DFT calculations, showing the accuracy of DFT predictions. Furthermore, the energy dispersive spectroscopy (EDS) maps in STEM (Figures 1C–1I) demonstrate uniform distributions of metal elements in the 3–9HEB samples on the nanometer scale with nearly equal atomic ratios (taking the 4HEB, 8HB, and 9HEB samples as examples, as listed in Table S2). These theoretical and experimental results verify the successful synthesis of single-phase 3–9HEB samples via the UHTS technique with engineered lattice distortion.

Improved electromagnetic wave absorption in HEBs by lattice distortion

To validate the electromagnetic wave absorption ability, the RL diagrams of the representative 9HEB samples are shown in Figures 2A and 2B (the others are provided in Figures S3 and S4). Among all HEBs, the 3HEB samples exhibit the narrowest EAB, covering merely 1.7 GHz at a considerable thickness of 4.6 mm. In contrast, the EAB of the 9HEB samples is the widest, reaching 7.2 GHz at a significantly reduced thickness of 1.5 mm, which is roughly 4-fold wider than that of the 3HEB samples. Meanwhile, the minimum RL value of the 3HEB samples has been calculated to be -24.6 dB, whereas that of the 9HEB samples is up to -42.6 dB. These measurements indicate that a dramatic improvement in electromagnetic wave absorption performance has been achieved solely by increasing lattice distortion in HEBs, which is associated with impedance matching and attenuation of electromagnetic waves. The impedance matching of the 3–9HEB samples was examined first. In general, $|Z_{in}/Z_0|$ values (where Z_{in} and Z_0 are the normalized input impedance and the impedance of free space, respectively) in the 0.8–1.2 range are considered ideal impedance matching,[4] which means electromagnetic waves

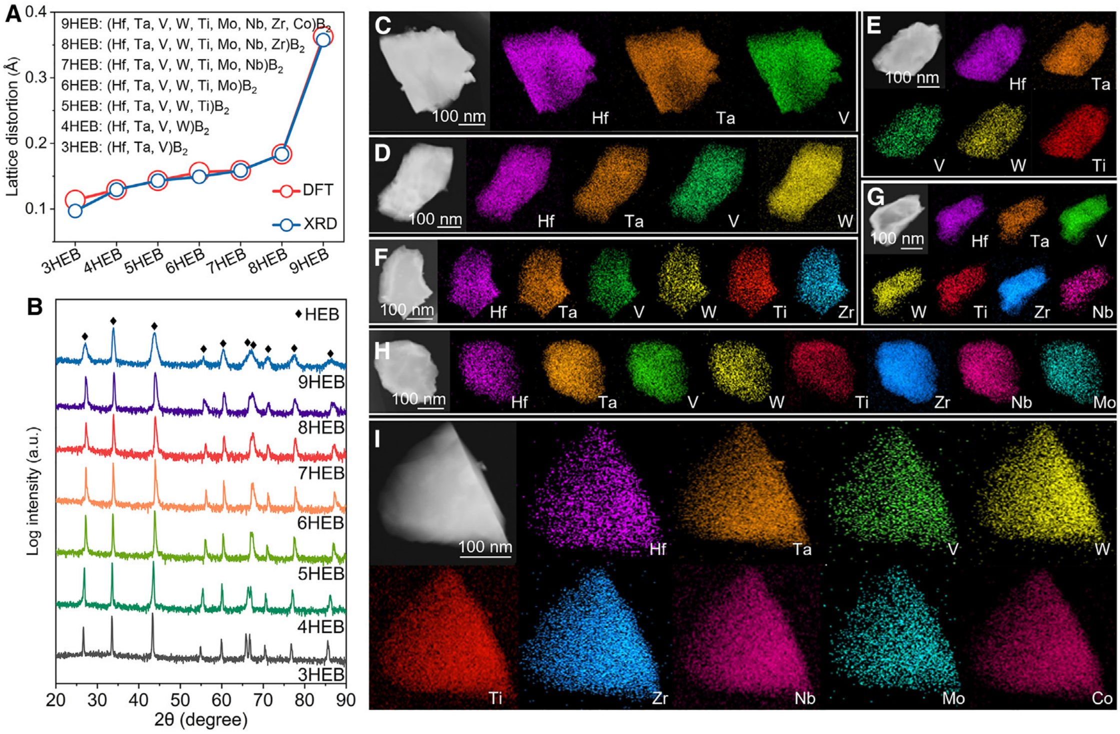

Figure 1. Lattice distortion, phase compositions, and elemental distributions of the 3–9HEB samples

(A) Lattice distortion calculated from DFT and XRD.

(B) XRD patterns.

(C–I) Elemental distributions of the 3–9HEB samples.

can enter the samples rather than being reflected. As illustrated in Figure S5, the impedance matching increases from 3HEB to 6HEB, implying an optimization of electromagnetic parameters by increasing lattice distortion. In terms of 7–9HEBs, their impedance matching is at a comparable level, suggesting that impedance matching is not the primary factor for the differences in their electromagnetic wave absorption performance.

The electromagnetic wave absorption capability of an absorbent is predominantly dominated by the relative complex permittivity ($\varepsilon_r = \varepsilon' - i\varepsilon''$) and permeability ($\mu_r = \mu' - i\mu''$). According to the electromagnetic theory, the real parts ε' and μ' are associated with the dielectric and magnetic storage, whereas the imaginary parts ε'' and μ'' represent the dielectric and magnetic dissipation, respectively.[8] Figure S6 shows that ε' and ε'' apparently increase when additional metal elements are included. To more intuitively demonstrate the dielectric loss ability of the 3–9HEB samples, their dielectric loss tangent ($\tan\delta_\varepsilon = \varepsilon'' / \varepsilon'$) was calculated. As displayed in Figure S7, the values of $\tan\delta_\varepsilon$ in the 3–9HEB samples rise monotonically with constituent metal elements increasing, suggesting a key role of lattice distortion in the dielectric loss of HEBs. Moreover, to investigate the reasons behind the improved dielectric loss in the representative 9HEB samples, their Cole-Cole diagrams with ϵ'' vs. ϵ' are shown in Figure 2C. Generally, a single semicircle represents a Debye relaxation process, indicating energy dissipation of electromagnetic waves through polarization loss. Since 9HEB exhibits more semicircles than the other HEBs (Figure S8), it is reasonable to speculate that polarization relaxation occurs more frequently in the 9HEB samples. Besides, the long trailing tail observed in Figure 2C suggests that electron migration or hopping has happened in the 9HEB samples, implying a contribution of conduction loss to the electromagnetic wave absorption of 9HEB. It is worth noting that, except for the 7-9HEB samples, no significant trailing tails are found for the other HEB samples, indicating limited conduction loss that is closely connected to their relatively low σ. With regard to the magnetic dissipation abilities of the 3–9HEB samples, it is obvious that μ' and μ'' have no significant correlation with the constituent components since their values show a fluctuation trend as metal elements increase (Figure S9). It is also noteworthy that the μ'' values of these samples are all approaching zero, showing limited magnetic dissipation. Taking into account both the electric loss and magnetic loss, the collective electromagnetic wave attenuation constant (α) of the 3–9HEB samples was evaluated (the details regarding the calculation of α can be found under methods). As shown in Figure 2D, the α values increase monotonically from 3HEB to 9HEB, demonstrating the critical effects of lattice distortion on the electromagnetic wave attenuation capacity in HEBs. The EAB values of the 3–9HEB samples are presented in Figure 2E. Particularly, the developed 9HEB materials with the most severe lattice distortion show superior electromagnetic wave absorption performance compared to other single-component material systems, including carbides,[5,30–33] diborides,[34,35] oxides,[36–38] sulfides,[39–42] HECs,[26,30,43–46] HEOs,[28,47] HEBs,[48–50] high-entropy sulfides (HESs),[51,52] MAX phases,[27,53,54] graphene,[55,56] and MXene,[57–61] as illustrated in Figure 2F and Table S3. Based on

Please cite this article in press as: Gu et al., Lattice distortion boosted exceptional electromagnetic wave absorption in high-entropy diborides, Matter (2025), https://doi.org/10.1016/j.matt.2025.102004

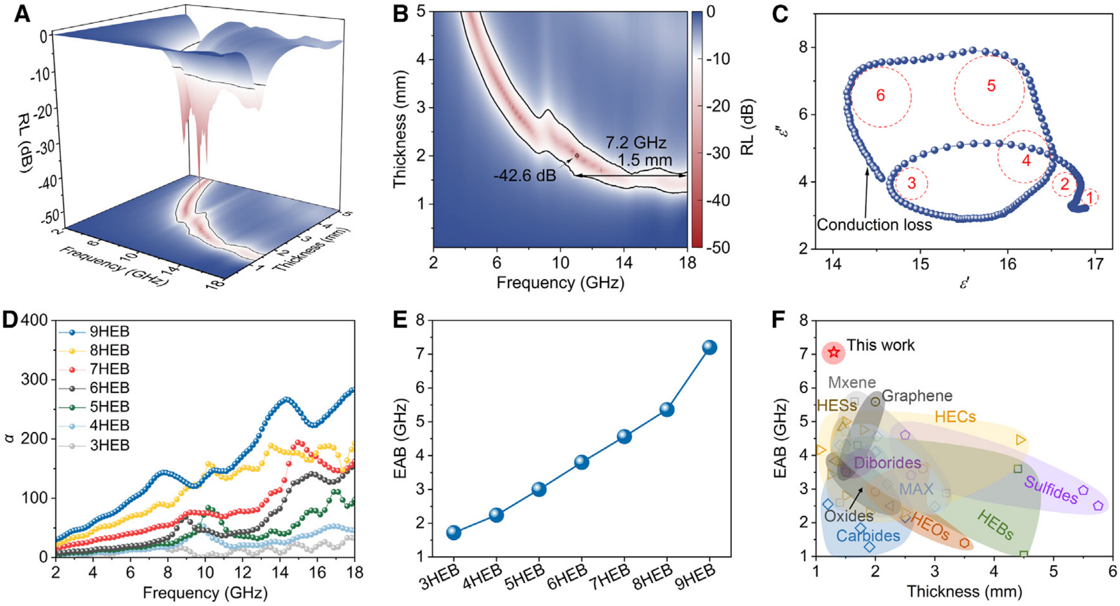

Figure 2. Electromagnetic wave absorption performance of the HEB samples

(A) Three-dimensional RL diagram of the representative 9HEB samples.

(B) Top view of (A).

(C) Cole-Cole diagram of the 9HEB samples with ε' and ε''.

(D) α as a function of frequency of the 3–9HEB samples.

(E) Summarized EAB of the 3–9HEB samples.

(F) EAB vs. thickness of the representative 9HEB and other reported single-phase absorbents, such as carbides,[5,30–33] diborides,[34,35] oxides,[36–38] sulfides,[39–42] HECs,[26,30,43–46] HEOs,[28,47] HEBs,[48–50] HESs,[51,52] MAX phases,[27,53,54] graphene,[55,56] and MXene.[57–61]

these results, it can be concluded that lattice distortion indeed promotes the electromagnetic wave absorption of HEBs. This promotion primarily arises from three key electromagnetic wave absorption mechanisms: lattice distortion-induced metal vacancies that exacerbate dipole polarization loss and conduction loss as well as lattice distortion-induced nanoclusters that enhance interfacial polarization loss. We discuss these mechanisms in detail later.

To further verify the direct relationship between lattice distortion and the electromagnetic wave absorption ability of HEBs, it is critical to rule out the impact of chemical compositions in HEBs. Since conduction loss is typically related to σ of absorbents,[3] we designed six types of 3HEBs, $(Hf_{1/3}Ta_{1/3}X_{1/3})B_2$ (X = Zr, Nb, Mo, Ti, W, and V; denoted as 3HEB-Zr, 3HEB-Nb, 3HEB-Mo, 3HEB-Ti, 3HEB-W, and 3HEB-V, respectively), to eliminate the effects of intrinsic σ of individual diborides on electromagnetic wave absorption abilities of HEBs. The XRD patterns (Figure S10A), Rietveld refinements (Figure S11), and atomic-resolution STEM imaging (Figure S12) confirm that all 3HEB samples are single-phase solid solutions with hexagonal structures. The σ values of individual diborides (ZrB_2, NbB_2, MoB_2, TiB_2, WB_2, and VB_2) were also measured (Figure S10B). It is apparent that, among all individual diborides, ZrB_2 exhibits the highest σ value (4.2×10^5 S m^{-1}), while WB_2 displays the lowest one (0.7×10^5 S m^{-1}). However, as depicted in Figure S10C, the 3HEB-V samples possess the best electromagnetic wave absorption ability with the widest EAB of 1.7 GHz. Conversely, the electromagnetic wave absorption performance of the 3HEB-Mo samples is the worst, with the narrowest EAB of 0.8 GHz (the electromagnetic parameters are provided in Figure S13, and the RL diagrams are shown in Figures S14 and S15). Notably, the electromagnetic wave absorption abilities of HEBs do not exhibit a substantial correlation with σ of individual diborides; instead, they strictly follow the trend in lattice distortion of the 3HEBs from DFT and XRD, as illustrated in Figure S10C. This result confirms that lattice distortion is the determinator for the electromagnetic wave absorption abilities of HEBs rather than σ of their individual diborides.

To eliminate the magnetic properties of individual diborides on the electromagnetic wave absorption abilities of HEBs, we synthesized three types of 4HEBs: $(Hf_{1/4}Ta_{1/4}V_{1/4}X_{1/4})B_2$ (X = Cr, Fe, and Co; abbreviated as 4HEB-Cr, 4HEB-Fe, and 4HEB-Co, respectively). According to the XRD patterns in Figure S16A, Rietveld refinements in Figure S17, and atomic-resolution STEM imaging in Figure S18, it is verified that single-phase 4HEBs were successfully synthesized without the formation of secondary phases. Moreover, the magnetic properties of individual monoborides (CrB, FeB, and CoB) were measured via a vibrating sample magnetometer (VSM), and their hysteresis loops are given in Figure S16B. Obviously, upon reaching an applied magnetic field of approximately 5,000 Oe, all samples attain saturation magnetization, indicating ferromagnetic behaviors.[62] In particular, the saturation magnetization of CrB is the highest (7.1 emu g^{-1}), followed by FeB (4.7 emu g^{-1}) and CoB (3.6 emu g^{-1}). In terms of coercive force, the values for CrB, FeB, and CoB are found to be 16.8, 16.9, and 17.0 Oe, respectively (Figure S16B, inset). Based on these experimental results, CrB has been proven to possess the strongest magnetism. Then, the Cr, Fe, and Co elements were

Please cite this article in press as: Gu et al., Lattice distortion boosted exceptional electromagnetic wave absorption in high-entropy diborides, Matter (2025), https://doi.org/10.1016/j.matt.2025.102004

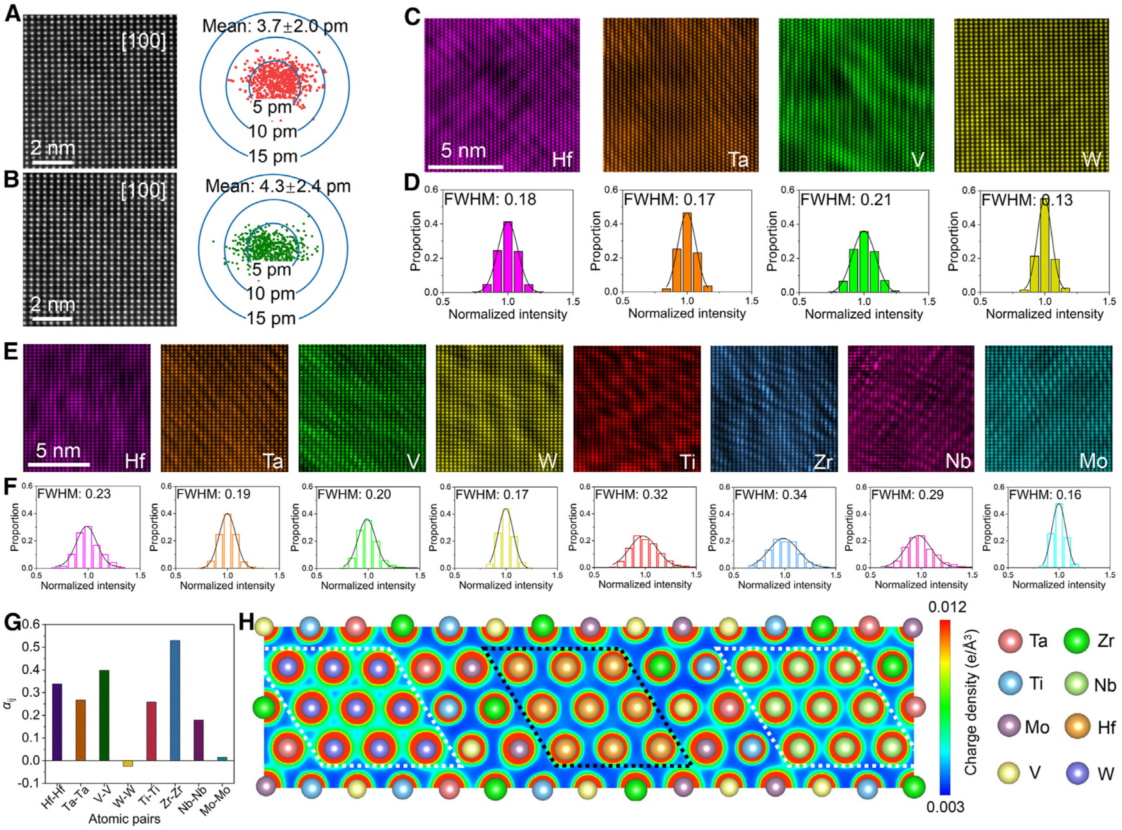

Figure 3. Atomic structures and chemical maps of the 4HEB and 8HEB samples

(A and B) Atomic-resolution HAADF-STEM images along the [100] zone axis and corresponding atomic displacements of 4HEB and 8HEB samples.

(C and D) Atomic-resolution STEM-EDS elemental images and the corresponding intensity statistics in the 4HEB samples. Image intensity was normalized by the mean value for intensity statistics in (D), where the histogram was fitted by Gaussian distribution, and the fluctuation of elements was defined by the FWHM.

(E and F) Atomic-resolution STEM-EDS elemental image and the corresponding intensity statistics in the 8HEB samples. Image intensity was normalized by the mean value for intensity statistics in (F), where the histogram was fitted by Gaussian distribution, and the fluctuation of elements was defined by the FWHM.

(G) First nearest-neighbor α_{ij} in 8HEB.

(H) Charge density distribution of the 8HEB model from DFT calculations.

included in the 4HEBs, and their electromagnetic wave absorption properties were evaluated. The electromagnetic parameters and corresponding RL diagrams are displayed in Figures S19 and S20, from which EAB of the 4HEB-Cr samples was measured to be 2.3 GHz, smaller than that of the 4HEB-Co samples (3.5 GHz) (Figure S16C). Combined with the magnetic testing results, it is evident that there is no direct significant connection between the electromagnetic wave absorption of HEBs and the magnetic properties of their individual components. Consequently, lattice distortion in HEBs is still identified to be essential in their electromagnetic wave absorption, as evidenced by the consistent changes between lattice distortion and EAB in these designed 4HEBs.

Exacerbated interfacial polarization loss by lattice distortion

To further elucidate the key effects of lattice distortion on the electromagnetic wave absorption performance, we investigated the atomic structure of HEBs with high-angle annular dark field (HAADF) imaging in STEM mode. The high-resolution HAADF-STEM images along the [100] zone axis show similar lattice structures of the 4HEB and 8HEB samples (Figures 3A, 3B, and S21). Lattice distortion, according to the displacement of atomic sites, was determined using the method of displacement separation analysis on HAADF images.[63] It is found that the mean atomic displacement is enlarged from the 3.7 pm of 4HEB to the 4.3 pm of 8HEB, indicating the enhancement of lattice distortion by including more elements in HEBs. Such enlarged lattice distortion also leads to a stronger strain fluctuation (Figures S22 and S23), where 8HEB exhibits a more pronounced strain fluctuation compared to that of 4HEB. These observations provide direct evidence of the augmentation in lattice distortion of HEBs with more metal elements, which may be attributed to the inhomogeneous distribution of elements on the atomic scale due to the mismatch of element characteristics and the complex chemical bonding of combined elements in high-entropy materials.[64],[65] Therefore, atomic-resolution STEM-EDS mapping was performed on HEBs to investigate the distributions of elements in atomic sites. Figures 3C–3F show the atomic-resolution STEM-EDS images of the 4HEB and 8HEB samples with clear and periodic distributions of combined elements in lattice structure along the [100] zone axis

Please cite this article in press as: Gu et al., Lattice distortion boosted exceptional electromagnetic wave absorption in high-entropy diborides, Matter (2025), https://doi.org/10.1016/j.matt.2025.102004

(Figure S24). It is notable that the intensity of an individual spot in the EDS image is roughly proportional to the concentration of a specific element in the atomic column; therefore, the intensity variation of atomic-resolution EDS spectrum images can be used to estimate the local concentration fluctuation of elements. Unlike the uniform elemental distributions on the scale of hundreds of nanometers (Figures 1C–1I), metal elements with similar overall atomic ratios (Table S2) in the 4HEB samples (Figure 3C) show the enrichment and deficiency in different atomic sites. The fluctuation of each constituent element was further calculated by the intensity statistics of all atomic columns in the corresponding EDS elemental maps (Methods). As summarized in Figure 3D, the fluctuations (determined by full width at half maximum [FWHM] values in the intensity statistics) of these elements have been calculated to range from 0.13 to 0.21 in 4HEB. The local concentration fluctuation of elements is also demonstrated in the atomic-resolution STEM-EDS images of 8HEB (Figure 3E), where more pronounced elemental fluctuations are found in this material with a range of 0.16–0.34 (Figure 3F). This indicates that local chemical fluctuations increase with enlarged lattice distortion due to the combination of more elements in HEB systems, which can be considered heterogeneous "nanoclusters" with coherent interfaces. This result can be confirmed by calculating the Warren-Cowley parameter (α_{ij}) in the first nearest-neighbor shell using molecular dynamics simulations,[66] which is a statistical measure to quantify the deviation of the actual atomic concentration in a given shell from the bulk concentration for the selected atomic pairs *i*-*j*. The statistics of α_{ij} in Figure 3G prove that the Zr-Zr has the strongest tendency to segregate at the atomic scale (with the α_{ij} value of 0.53), consistent with its highest FWHM value in the EDS maps. By contrast, $\alpha_{\text{W-W}}$ and $\alpha_{\text{Mo-Mo}}$ have relatively low values, suggesting that these two elements tend to be distributed homogeneously in the lattice. More detailed information is presented in Table S4. To clarify the effects of these nanoclusters on the interfacial polarization of HEBs, their charge density distribution was investigated using DFT. As shown in Figure 3H, for specific nanoclusters, such as W- and Nb-rich ones, there is significant electronic charge accumulation. Meanwhile, other nanoclusters (e.g., Hf-rich nanoclusters), have a relatively low electronic charge density, leading to an inhomogeneous charge density distribution in 8HEB. In addition to the charge density, the work function is also critical for the interfacial polarization.[3] To facilitate further analyses, these nanoclusters were simplified to specific individual diborides, and their work functions were calculated. As shown in Figure S25, the work functions are variable based on the types of diborides. In particular, the value for HfB_2 is the lowest (3.1 eV for the (100) plane), while that for WB_2 is the highest (4.7 eV for the (100) plane). Such significant differences demonstrate that, upon electrons moving to the interfaces of nanoclusters, these nanointerfaces can serve as barriers to impede the further transport of electrons, leading to the separation of positive and negative charges on either side of the interfaces and, thereby, exacerbating interfacial polarization.

Enhanced conduction loss and dipole polarization loss by lattice distortion

Besides interfacial polarization, lattice distortion may help to improve conduction loss in HEBs. As displayed in Figure 4A, with the constituent elements increasing, the σ values of the 3–9HEB samples rise markedly from 2.3×10^5 S m^{-1} to 12.8×10^5 S m^{-1}, indicating the advantageous influence of lattice distortion on σ of HEBs. Combining the Cole-Cole diagrams shown in Figure 2C and Figure S8, we speculate that the σ value of the 7HEB samples (approximately 8.7×10^5 S m^{-1}) may represent the threshold at which significant conduction loss occurs in HEB systems. Vacancy concentrations were then measured by an electron paramagnetic resonance (EPR) spectrometer to increase from 7.2×10^{13} spins g^{-1} to 23.7×10^{13} spins g^{-1} for the 3–9HEB samples (Figure S26), showing a consistent change trend with σ. To identify the specific elemental deficiencies, the vacancy formation energy for all elements in the 8HEB system was computed. It can be seen in Figure 4B that the Ta element is the most prone to loss owing to its lowest vacancy formation energy (−8.3 eV), followed by the Hf, Zr, Nb, Ti, V, W, and Mo elements. Notably, formation of the B vacancy is particularly difficult due to its highest vacancy formation energy (1.3 eV). The atomic-resolution STEM imaging and corresponding intensity measurement clearly demonstrate the presence of vacancies in cation sites (Figures 4C and 4D), confirming the loss of some metal atoms as a result of their low vacancy formation energy. To investigate the effects of metal vacancies on σ of the 8HEB samples, the Ta element with the lowest vacancy formation energy was taken as an example. To clarify the effects of metal vacancy on σ of HEBs, Figure 4E illustrates the density of state (DOS) in the 8HEB system near the Fermi level with different Ta vacancy concentrations (V_{Ta}). The DOS at the Fermi level rises from 0.62 states eV^{-1} atom^{-1} to 0.84 states eV^{-1} atom^{-1} with the V_{Ta} increasing from 0% to 3.1%, indicating an increased metallicity that is beneficial to the improvement of σ. It is known that, when the electromagnetic waves travel through an absorbent, energy can convert into electric current. With an enhanced σ, electronic transport within the lattices can accelerate, resulting in the generation of additional Joule heat to consume electromagnetic wave energy. In addition to conduction loss, metal vacancies can also give rise to dipole polarization loss. Figure 4F shows the differential charge density distribution of the 8HEB system via DFT. Clearly, a typical Ta vacancy can induce significant electronic rearrangement, leading to an uneven distribution of positive and negative charges. As a result, when subjected to an alternating electric field, vacancy-induced dipolar polarization and relaxation processes can occur frequently, leading to significant consumption of electromagnetic wave energy.

Overall, these experimental and theoretical results provide compelling evidence that lattice distortion can improve the electromagnetic wave absorption performance of HEBs through three key mechanisms, as briefly illustrated in Figure 5. Firstly, significant lattice distortion creates numerous metal vacancies. In this case, Ta vacancies are energetically preferable to form, enhancing the metallicity of HEBs by increasing the DOS at the Fermi level. This enhancement can raise σ of HEBs, thereby promoting their conduction loss. Second, metal vacancies originating from significant lattice distortion result in the formation of numerous dipoles in their vicinity. Consequently, as incident electromagnetic waves interact with HEBs, their energy can be substantially dissipated through frequent reorientation of these dipoles, leading to increased dipole polarization loss.

Please cite this article in press as: Gu et al., Lattice distortion boosted exceptional electromagnetic wave absorption in high-entropy diborides, Matter (2025), https://doi.org/10.1016/j.matt.2025.102004

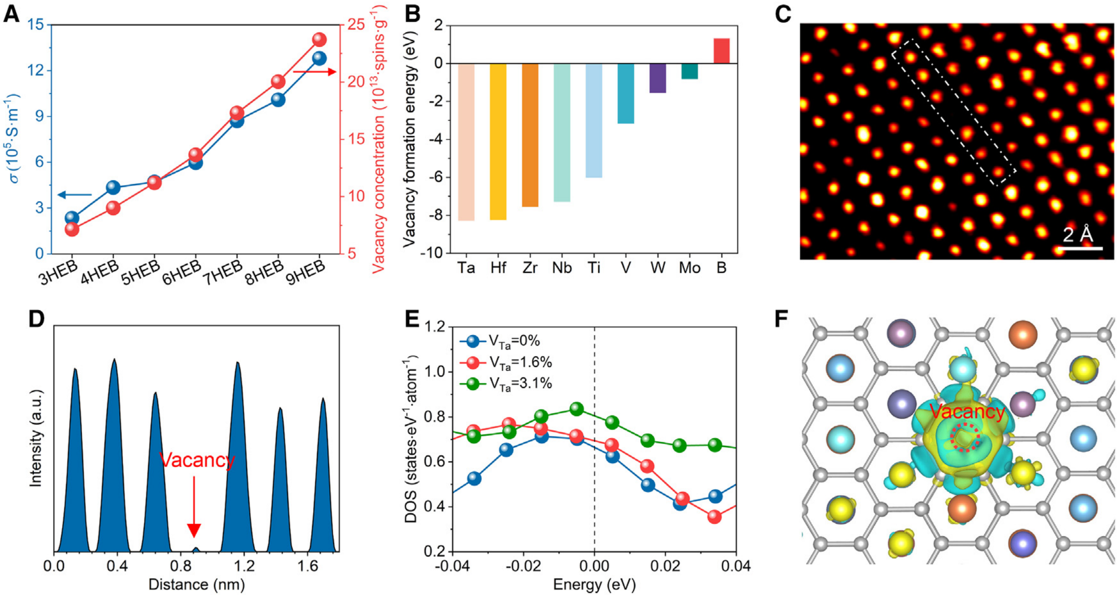

Figure 4. Metal vacancy measurements and overall electromagnetic wave absorption mechanisms

(A) σ and vacancy concentration of the 3–9HEB samples.

(B) Vacancy formation energy of metal elements in the 8HEB system.

(C) Atomic-resolution HAADF-STEM image of the 8HEB samples.

(D) Intensity profile of the region marked in (C).

(E) DOS of the 8HEB structure with different V_{Ta}.

(F) Differential charge density distribution of the 8HEB structure with a vacancy of the Ta element. The value of the isosurface level is ±0.0022 e/Bohr.[3] Yellow and green regions represent the decrease and increase in electronic charges, respectively.

Third, severe lattice distortion introduces substantial elemental fluctuations at the atomic scale. For instance, the Zr element has the strongest tendency to segregate in the 9HEB system, as evidenced by its highest α_{ij}. This segregation gives rise to pronounced elemental fluctuations, which can be considered as diverse heterogeneous nanoclusters with coherent interfaces. As a result, when electrons move and encounter the interfaces of these nanoclusters (with significantly different work functions), they can act as barriers to impede electron transport. This phenomenon results in the separation of positive and negative charges on either side of the interfaces, therefore increasing interfacial polarization loss.

Conclusions

We present a universal and effective lattice distortion engineering strategy to realize remarkable electromagnetic wave absorption in HEBs. Specifically, we tailor lattice distortion by incrementally introducing metal elements into the 3-9HEB samples using the UHTS technique. The experimental and theoretical results demonstrate that lattice distortion can boost the electromagnetic wave absorption performance of HEBs through three key absorption mechanisms: (1) lattice distortion leads to the formation of abundant metal vacancies, dramatically increasing σ of HEBs and so facilitating conduction loss; (2) lattice distortion-induced metal vacancies generate numerous dipoles, giving rise to significant dipole polarization loss; and (3) lattice distortion results in the formation of diverse nanoclusters functioning as barriers to exacerbate interfacial polarization loss. Benefitting from these unique electromagnetic wave absorption mechanisms, our 9HEB materials with the greatest lattice distortion achieve a broad EAB of 7.2 GHz at an ultralow thickness of 1.5 mm, showing superior electromagnetic wave absorption performance compared to other single-phase absorbents. This study presents an effective pathway for significantly improving the electromagnetic wave absorption in ceramics.

METHODS

Sample synthesis

All chemicals were used as received without further purification. Commercial metal oxides, including HfO_2, Ta_2O_5, Nb_2O_5, ZrO_2, TiO_2, V_2O_5, MoO_3, WO_3, Cr_2O_3, Fe_2O_3, and Co_2O_3 (purity, 99.9%; particle size, 1–3 μm; McLean Biochemical Technology, China), and amorphous B_4C powders (purity, 99%; particle size, 10–20 μm, McLean Biochemical Technology) were used as raw materials. First, the metal oxides were equimolarly weighed and mixed with 30%-excess B_4C powders based on the ratio of the reaction equation for 24 h. Subsequently, the mixed powders were pressed into pellets (16 × 16 × 3 mm^3) under a pressure of 10 MPa and a holding time of 3 min. These pellets were then placed between two pieces of the graphite heater (100 × 18 × 5 mm^3; AvCarb Felt G475, Fuel Cell Store, USA) of our self-developed UHTS apparatus.[67] Afterward, an alternating current (100–250 A) was applied to both ends of the heater to heat the pellets to 2,000°C ± 100°C under the protection of Ar gas at atmospheric pressure. The heating rate and holding time were set to be

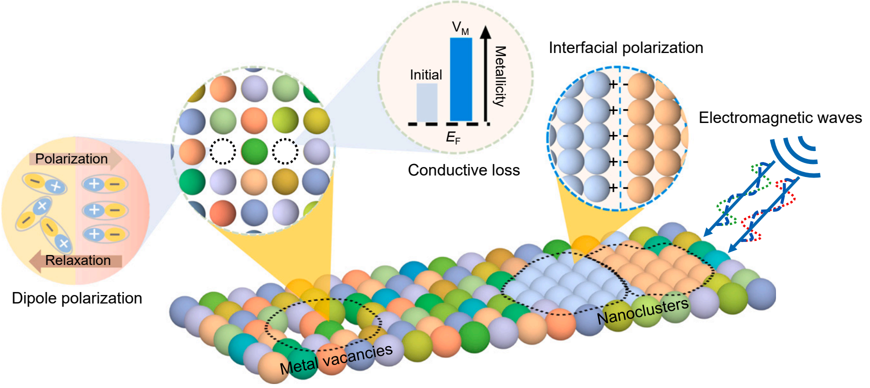

Figure 5. Schematic of electromagnetic wave absorption mechanisms in HEBs with severe lattice distortion

Lattice distortion-induced metal vacancies facilitate conduction loss and dipole polarization loss, and lattice distortion-induced nanoclusters cause significant interfacial polarization loss. E_F and V_M represent the energy at the Fermi level and metal vacancy, respectively.

50–80 K s^{-1} and 40 s, respectively. All HEBs were synthesized under the same conditions. After naturally cooling down to room temperature, the pellets were taken out, ground for 30 min, and sifted through a 300-mesh sieve to obtain HEB powders. Finally, these HEB powders were uniformly blended with paraffin with a weight ratio of 3:7 at 85°C for 30 min. After natural cooling, the samples were machined into concentric rings with dimensions of 3.04 mm inner diameter, 7.00 mm outer diameter, and 3 mm thickness.

Characterization

Phase compositions of the samples were tested by XRD (X'pert PRO, PANalytical, the Netherlands), and the resultant patterns were further refined using a general structure analysis system software. The electromagnetic parameters of the samples were measured by a vector network analyzer (E5071C, Agilent Technologies, USA) in the range of 2–18 GHz. The RL values of the samples were calculated based on the transmission line theory as follows[5]:

$$RL = 20\,log\left|\frac{Z_{in} - Z_0}{Z_{in} + Z_0}\right| \qquad \text{(Equation 1)}$$

$$Z_{in} = Z_0\sqrt{\frac{u_r}{\varepsilon_r}}tanh\left[j\left(\frac{2\pi fd}{c}\right)\sqrt{u_r\varepsilon_r}\right] \qquad \text{(Equation 2)}$$

where Z_{in} and Z_0 are the normalized input impedance and the impedance of free space, respectively; ε_r and μ_r are the complex permittivity and permeability, respectively; f and c are the incident electromagnetic wave frequency and speed of light, respectively; and f is the thickness of the tested sample. α of the samples was computed according to the following equation[7]:

$$\alpha = \frac{\sqrt{2}\pi f}{c} \times \sqrt{(\mu''\varepsilon'' - \mu'\varepsilon') + \sqrt{(\mu''\varepsilon'' - \mu'\varepsilon')^2 + (\mu'\varepsilon'' + \mu''\varepsilon')^2}} \qquad \text{(Equation 3)}$$

where f is the frequency, and c is the speed of light. σ of the samples (densified to 98% by a spark plasma sintering apparatus; LABOX-225, Sinterland, Japan) was tested by a four-probe resistance system (280SI, Four Dimensions, USA). The magnetization of the samples (5 mm in width × 12 mm in length) was tested by a VSM (Dynacool-9, Quantum Design, USA) under a magnetic field of 5 T. Vacancy concentrations of the samples were measured by an EPR spectrometer (EMXplus-6/1, Bruker, Germany).

STEM measurements of the as-synthesized HEB materials were performed on a double Cs-corrected TEM (Titan Themis G2, FEI, USA) with a Super-X EDS detector operated at 300 kV. Atomic structures of the samples were investigated by HAADF imaging in STEM mode with a probe convergence angle of 25 mrad and a collection angle of 61–200 mrad. To accurately determine the atomic displacement of lattice structures in HEB samples, the drift distortion of high-resolution HAADF-STEM images was corrected by orthogonal image pairs.[68] The center of atomic sites (with a number of approximately 600) in the STEM images was determined by a 2D Gaussian fitting algorithm in the CalAtom software.[69] The atomic displacement was determined by displacement separation analysis, which can directly separate atomic displacements from the lattice structure without prior knowledge based on Fourier space filtering.[63] The geometric phase analysis was used to obtain the strain maps of atomic-resolution STEM images with a commercial plugin (HREM Research). Atomic-resolution EDS maps (400 × 400 pixels) of HEB samples were acquired in the STEM mode with a dwell time of 8 µs and a pixel size of 25.65 pm. The total acquisition time was around 35 min. The beam current was roughly 50 pA for both HAADF images and EDS maps. The raw EDS spectrum images were generated in Velox software (v.3.9) with the characteristic X-ray signals of each element (Ti Kα, V Kα, Zr Kα, Nb Kα, Mn Kα, Hf Lα, Ta Lα, and W Lα). Then, these raw EDS maps were denoised using non-local principal-component analysis (the detailed denoised procedure has been described previously[64]), which enabled the accurate determination of the atomic position and intensity in denoised EDS images. The intensity of atomic sites (with a number of approximately 1,000) in denoised EDS images was determined by CalAtom software with the same fitting algorithm as used in atomic-resolution STEM images.

Calculation

The chemical frustration was evaluated by the α_{ij} at the first nearest-neighbor shell using molecular dynamics simulations[66]:

$$\alpha_{ij} = \frac{p_{ij} - c_j}{\delta_{ij} - c_j} \qquad \text{(Equation 4)}$$

where p_{ij} is the average probability of finding a type j atom around a central i-type atom, c_j is the average concentration of

Please cite this article in press as: Gu et al., Lattice distortion boosted exceptional electromagnetic wave absorption in high-entropy diborides, Matter (2025), https://doi.org/10.1016/j.matt.2025.102004

j-type atoms in the system, and δ_{ij} is the Kronecker delta function. A near-zero α_{ij} suggests a random solid solution. For the same species pairs (i.e., $i = j$), a positive α_{ii} indicates attractive interactions of *i*-type atoms (segregation) in the first nearest-neighbor shell, while a negative value means repulsion. In contrast, for pairs of different elements, a negative α_{ij} suggests the tendency of *j*-type atoms to cluster around type *i* atoms, while a positive value means the opposite.

First-principles calculations were adopted via the Vienna Ab initio Simulation Package based on the DFT with the projector-augmented wave pseudopotentials[70] and the Perdew-Burke-Ernzerhof[71] version of the generalized gradient approximation.[72] According to the TiB_2 conventional cell with a space group of *P*6/*mmm*, the chemically disordered HEB models were generated by the special quasi-random structure[73] approach in the Alloy Theoretic Automated Toolkit,[74] while the HEB models with metal nanoclusters were generated intentionally. The cutoff energy for all calculations was set to 420 eV. The energy convergence criterion of the electronic self-consistency cycle was 10^{-5} eV, and the atomic structure relaxed until the force on each atom was less than 0.01 eV/Å. In addition, a spacing of 0.3 $Å^{-1}$ with the Γ-centered mesh was used in Brillouin zones. Lattice distortion was calculated as follows[75]:

$$\bar{\mu} = \frac{2\sqrt{\sum_{i}^{n}\left(a_i^{\mathrm{eff}} - \bar{a}\right)^2} + \sqrt{\sum_{i}^{n}\left(c_i^{\mathrm{eff}} - \bar{c}\right)^2}}{3} \qquad \text{(Equation 5)}$$

where a_i^{eff} and c_i^{eff} are the effective lattice constants of the *i*-th element, $\bar{a}$ and $\bar{c}$ are the average interatomic distances of *n* constituent diborides, and *n* is the number of constituent metal elements in the HEBs. The effective interatomic distances of the a_i^{eff} and c_i^{eff} were obtained by

$$a_i^{\mathrm{eff}} = \sum_{j}^{n} f_j \left(1 + \frac{\Delta V_{ij}}{V_i}\right)^{1/3} a_i \qquad \text{(Equation 6)}$$

$$c_i^{\mathrm{eff}} = \sum_{j}^{n} f_j \left(1 + \frac{\Delta V_{ij}}{V_i}\right)^{1/3} c_i \qquad \text{(Equation 7)}$$

where f_j is the atomic fraction, V_i is the volume of the *i*-th diboride, a_i and c_i are the lattice constants of the individual diboride corresponding to the *i*-th element, and ΔV_{ij} is the change of the lattice volume of the *i*-th element dissolving into the *j*-th element, which can be expressed as[76]

$$\Delta V_{ij} = \frac{V_{\text{after solid solution}} - V_{\text{before solid solution}}}{N} \qquad \text{(Equation 8)}$$

where the $V_{\text{before solid resolution}}$ and $V_{\text{after solid resolution}}$ are supercell volumes of *i*-th diboride before and after optimization, respectively, and the *N* is the number of solvable elements corresponding to the half number of metal atoms in the diboride supercells. $\bar{\mu}$ can also be obtained from XRD refinement by replacing $\bar{a}$ and $\bar{c}$ with the corresponding analyzed lattice parameters. The formation energy of a defect *X* in the HEB model was calculated by the following equation[77]:

$$E_f[X] = E_{\mathrm{tot}}[X] - E_{\mathrm{tot}}[bulk] + E_X \qquad \text{(Equation 9)}$$

where $E_{\mathrm{tot}}[X]$ and $E_{\mathrm{tot}}[bulk]$ are the total energy derived from defective and perfect HEB models, respectively. E_X refers to the energy of the *X* atom in its ground state. In addition, the charge density difference was computed via the following equation[78]:

$$\Delta\rho = \rho_{\mathrm{tot}}[bulk] - \rho_{\mathrm{tot}}[Me] - \rho_{\mathrm{Me}} \qquad \text{(Equation 10)}$$

where $\rho_{\mathrm{tot}}[bulk]$ stands for the charge density of the perfect HEB models, and $\rho_{\mathrm{tot}}[Me]$ and ρ_{Me} are the charge densities derived from the defective HEB model and the defective metal atom, respectively.

RESOURCE AVAILABILITY

Lead contact

Requests for further information and resources should be directed to and will be fulfilled by the lead contact, Yanhui Chu (chuyh@scut.edu.cn).

Materials availability

All HEB samples used in this study are available upon request from the Chu lab at South China University of Technology.

Data and code availability

All data supporting this study are available in the manuscript and supplemental information.

ACKNOWLEDGMENTS

The authors acknowledge financial support from the National Natural Science Foundation of China (52122204, 52472072, and 52302262) and the Guangdong Natural Science Foundation (2024A1515010020).

AUTHOR CONTRIBUTIONS

Supervision, Y.C.; investigation, F.G., L.Z., W.W., and Y.C.; calculation, H.M., Y.L., and H.Y.; writing – original draft, L.Z. and W.W.; writing – review & editing, H.Y. and Y.C. All authors contributed helpful discussions.

DECLARATION OF INTERESTS

The authors declare no competing interests.

SUPPLEMENTAL INFORMATION

Supplemental information can be found online at https://doi.org/10.1016/j.matt.2025.102004.

Received: October 15, 2024
Revised: November 28, 2024
Accepted: January 23, 2025
Published: February 18, 2025

REFERENCES

1. Shahzad, F., Alhabeb, M., Hatter, C.B., Anasori, B., Man Hong, S., Koo, C.M., and Gogotsi, Y. (2016). Electromagnetic interference shielding

with 2D transition metal carbides (MXenes). Science *353*, 1137–1140. https://doi.org/10.1126/science.aag2421.

2. Lqbal, A., Shahzad, F., Hantanasirisakul, K., Kim, M.K., Kwon, J., Hong, J., Kim, H., Kim, D., Gogotsi, Y., and Koo, C.M. (2020). Anomalous absorption of electromagnetic waves by 2D transition metal carbonitride Ti_3CNT_x (MXene). Science *369*, 446–450.
3. Qin, M., Zhang, L., and Wu, H. (2022). Dielectric loss mechanism in electromagnetic wave absorbing materials. Adv. Sci. *9*, 2105553.
4. Tang, Z., Xu, L., Xie, C., Guo, L., Zhang, L., Guo, S., and Peng, J. (2023). Synthesis of $CuCo_2S_4$@Expanded Graphite with crystal/amorphous heterointerface and defects for electromagnetic wave absorption. Nat. Commun. *14*, 5951. https://doi.org/10.1038/s41467-023-41697-6.
5. Zhao, R., Gao, T., Li, Y., Sun, Z., Zhang, Z., Ji, L., Hu, C., Liu, X., Zhang, Z., Zhang, X., and Qin, G. (2024). Highly anisotropic Fe_3C microflakes constructed by solid-state phase transformation for efficient microwave absorption. Nat. Commun. *15*, 1497.
6. Xu, X., Shi, S., Tang, Y., Wang, G., Zhou, M., Zhao, G., Zhou, X., Lin, S., and Meng, F. (2021). Growth of NiAl-layered double hydroxide on graphene toward excellent anticorrosive microwave absorption application. Adv. Sci. *8*, 2002658. https://doi.org/10.1002/advs.202002658.
7. Huang, W., Song, M., Wang, S., Wang, B., Ma, J., Liu, T., Zhang, Y., Kang, Y., and Che, R. (2024). Dual-step redox engineering of two-dimensional CoNi-alloy embedded B, N-doped carbon layers towards tunable electromagnetic wave absorption and light-weight infrared stealth heat insulation devices. Adv. Mater. *36*, 2403322. https://doi.org/10.1002/adma.202403322.
8. Yang, J., Wang, J., Li, H., Wu, Z., Xing, Y., Chen, Y., and Liu, L. (2022). MoS_2/MXene aerogel with conformal heterogeneous interfaces tailored by atomic layer deposition for tunable microwave absorption. Adv. Sci. *9*, 2101988. https://doi.org/10.1002/advs.202101988.
9. Wen, C., Li, X., Zhang, R., Xu, C., You, W., Liu, Z., Zhao, B., and Che, R. (2022). High-density anisotropy magnetism enhanced microwave absorption performance in $Ti_3C_2T_x$ MXene@Ni microspheres. ACS Nano *16*, 1150–1159. https://doi.org/10.1021/acsnano.1c08957.
10. Che, R., Peng, L., Duan, X., Chen, Q., and Liang, X. (2004). Microwave absorption enhancement and complex permittivity and permeability of Fe encapsulated within carbon nanotubes. Adv. Mater. *16*, 401–405. https://doi.org/10.1002/adma.200306460.
11. Ma, Z., Yang, K., Li, D., Liu, H., Hui, S., Jiang, Y., Li, S., Li, Y., Yang, W., Wu, H., and Hou, Y. (2024). The electron migration polarization boosting electromagnetic wave absorption based on Ce atoms modulated yolk@shell Fe_xN@NGC. Adv. Mater. *36*, e2314233. https://doi.org/10.1002/adma.202314233.
12. Xu, C., Liu, P., Wu, Z., Zhang, H., Zhang, R., Zhang, C., Wang, L., Wang, L., Yang, B., Yang, Z., et al. (2022). Customizing heterointerfaces in multilevel hollow architecture constructed by magnetic spindle arrays using the polymerizing-etching strategy for boosting microwave absorption. Adv. Sci. *9*, 2200804. https://doi.org/10.1002/advs.202200804.
13. Rost, C.M., Sachet, E., Borman, T., Moballegh, A., Dickey, E.C., Hou, D., Jones, J.L., Curtarolo, S., and Maria, J.P. (2015). Entropy-stabilized oxides. Nat. Commun. *6*, 8485. https://doi.org/10.1038/ncomms9485.
14. Ye, B., Wen, T., Nguyen, M.C., Hao, L., Wang, C.Z., and Chu, Y. (2019). First-principles study, fabrication and characterization of $(Zr_{0.25}Nb_{0.25}Ti_{0.25}V_{0.25})C$ high-entropy ceramics. Acta Mater. *170*, 15–23. https://doi.org/10.1016/j.actamat.2019.03.021.
15. Meng, H., Wei, P., Tang, Z., Yu, H., and Chu, Y. (2024). Data-driven discovery of formation ability descriptors for high-entropy rare-earth monosilicates. J. Materiomics. *10*, 738–747. https://doi.org/10.1016/j.jmat.2023.11.017.
16. Wen, Z., Tang, Z., Liu, Y., Zhuang, L., Yu, H., and Chu, Y. (2024). Ultrastrong and high thermal insulating porous high-entropy ceramics up to 2000 °C. Adv. Mater. *36*, 2311870. https://doi.org/10.1002/adma.202311870.
17. Tang, Z., Wen, Z., Liu, Y., Zhuang, L., Yu, H., and Chu, Y. (2024). Rapid experimental screening of high-entropy diborides for superior oxidation resistance. Adv. Funct. Mater. *34*, 2312239. https://doi.org/10.1002/adfm.202312239.
18. Ye, B., Wen, T., Huang, K., Wang, C.Z., and Chu, Y. (2019). First-principles study, fabrication, and characterization of $(Hf_{0.2}Zr_{0.2}Ta_{0.2}Nb_{0.2}Ti_{0.2})C$ high-entropy ceramic. J. Am. Ceram. Soc. *102*, 4344–4352. https://doi.org/10.1016/j.actamat.2019.03.021.
19. Kim, S.C., Wang, J., Xu, R., Zhang, P., Chen, Y., Huang, Z., Yang, Y., Yu, Z., Oyakhire, S.T., Zhang, W., et al. (2023). High-entropy electrolytes for practical lithium metal batteries. Nat. Energy *8*, 814–826. https://doi.org/10.1038/s41560-023-01280-1.
20. Yu, R., Liu, Y., Sun, X., He, G., Dong, H., Deng, S., Li, J., and Chu, Y. (2023). Composition engineering of high-entropy diboride nanoparticles for efficient catalytic degradation of antibiotics. Sci. China Mater. *66*, 3582–3591. https://doi.org/10.1007/s40843-023-2496-5.
21. Wen, T., Ye, B., Nguyen, M.C., Ma, M., and Chu, Y. (2020). Thermophysical and mechanical properties of novel high-entropy metal nitride-carbides. J. Am. Ceram. Soc. *103*, 6475–6489. https://doi.org/10.1007/s40145-022-0605-3.
22. Jiang, B., Yu, Y., Cui, J., Liu, X., Xie, L., Liao, J., Zhang, Q., Huang, Y., Ning, S., Jia, B., et al. (2021). High-entropy-stabilized chalcogenides with high thermoelectric performance. Science *371*, 830–834. https://doi.org/10.1126/science.abe1292.
23. Liu, Y., Zhu, Z., Tang, Z., Yu, H., Zhuang, L., and Chu, Y. (2024). Unraveling lattice-distortion hardening mechanisms in high-entropy carbides. Small *20*, 2403159. https://doi.org/10.1002/smll.202403159.
24. Lei, X., Tang, Q., Zheng, Y., Kidkhunthod, P., Zhou, X., Ji, B., and Tang, Y. (2023). High-entropy single-atom activated carbon catalysts for sustainable oxygen electrocatalysis. Nat. Sustain. *6*, 816–826. https://doi.org/10.1038/s41893-023-01101-z.
25. Ma, M., Sun, Y., Wu, Y., Zhao, Z., Ye, L., and Chu, Y. (2022). Nanocrystalline high-entropy carbide ceramics with improved mechanical properties. J. Am. Ceram. Soc. *105*, 606–613. https://doi.org/10.1111/jace.18100.
26. Zhou, Y., Zhao, B., Chen, H., Xiang, H., Dai, F.Z., Wu, S., and Xu, W. (2021). Electromagnetic wave absorbing properties of TMCs (TM = Ti, Zr, Hf, Nb and Ta) and high entropy $(Ti_{0.2}Zr_{0.2}Hf_{0.2}Nb_{0.2}Ta_{0.2})C$. J. Mater. Sci. Technol. *74*, 105–118. https://doi.org/10.1016/j.jmst.2020.10.016.
27. Chen, L., Li, Y., Zhao, B., Liu, S., Zhang, H., Chen, K., Li, M., Du, S., Xiu, F., Che, R., et al. (2023). Multiprincipal Element M_2FeC (M = Ti,V,Nb,Ta,Zr) MAX Phases with Synergistic Effect of Dielectric and Magnetic Loss. Adv. Sci. *10*, 2206877. https://doi.org/10.1002/advs.202206877.
28. Zhao, B., Yan, Z., Du, Y., Rao, L., Chen, G., Wu, Y., Yang, L., Zhang, J., Wu, L., Zhang, D.W., and Che, R. (2023). High-entropy enhanced microwave attenuation in titanate perovskites. Adv. Mater. *35*, 2210243. https://doi.org/10.1002/adma.202210243.
29. Liu, Y., Ma, M., Wang, W., Tang, H., Yu, H., Zhuang, L., Xie, P., and Chu, Y. (2024). Lattice distortion enhanced hardness in high-entropy borides. Adv. Funct. Mater. 2416992. https://doi.org/10.1002/adfm.202416992.
30. Zhang, J., Wang, W., Zhang, Z., Chen, J., Sun, X., Sun, G., Liang, Y., Han, G., and Zhang, W. (2023). Synthesis, microstructure and electromagnetic wave absorption properties of high-entropy carbide powders. J. Alloys Compd. *966*, 171593. https://doi.org/10.1016/j.jallcom.2023.171593.
31. Zhu, P., Kang, Y., Li, X., Yu, H., Liu, T., Song, M., Zhang, Y., Zhou, L., Zhao, P., and Huang, W. (2024). UV-modification of Ag nanoparticles on α-MoC_x for interface polarization engineering in electromagnetic wave absorption. Nanoscale *16*, 6249–6258. https://doi.org/10.1039/d3nr05917k.
32. Wang, Y., Luo, C., Wu, Y., Hu, X., Wang, L., Chen, X., Chao, M., Liu, G., Hu, Y., and Yan, L. (2023). High temperature stable, amorphous SiBCN microwave absorption ceramics with tunable carbon structures derived from divinylbenzene crosslinked hyperbranched polyborosilazane. Carbon *213*, 118189. https://doi.org/10.1016/j.carbon.2023.118189.

Please cite this article in press as: Gu et al., Lattice distortion boosted exceptional electromagnetic wave absorption in high-entropy diborides, Matter (2025), https://doi.org/10.1016/j.matt.2025.102004

33. Xu, R., Zhou, J., Huang, W., Yu, G., Guo, L., Huang, X., and Shao, G. (2024). Polymer-derived silicon oxycarbonitride bowls with hollow structures and hetero-nanodomains for electromagnetic wave absorption. J. Mater. Chem. C *12*, 4640–4647. https://doi.org/10.1039/d4tc00274a.

34. Wang, S., Bi, J., Liang, G., Yang, Y., Qiao, L., Yin, Z., Liang, S., Rong, J., and Che, C. (2024). Hafnium boride whiskers prepared by boro/carbothermal reduction for high-performance electromagnetic wave absorption. Ceram. Int. *50*, 5121–5131. https://doi.org/10.1016/j.ceramint.2023.11.256.

35. Wang, S., Bi, J., Liang, G., Yuan, J., Chen, Y., Qiao, L., Liang, S., Rong, J., and Che, C. (2023). Titanium boride fibers prepared by chloride-assisted carbothermic method for high-performance electromagnetic wave absorption. Ceram. Int. *49*, 26110–26118. https://doi.org/10.1016/j.ceramint.2023.05.167.

36. Zhou, B., Ke, X., Zhou, Q., and Cui, Y. (2024). Constructing three-dimensional wool-spherical vanadium-doped Nb_2O_5 microspheres with superior electromagnetic absorption performance. Mater. Res. Bull. *174*, 112724. https://doi.org/10.1016/j.materresbull.2024.112724.

37. Greena, M., Tran, A., Smedley, R., Roach, A., Murowchick, J., and Chen, X. (2019). Microwave absorption of magnesium/hydrogen-treated titanium dioxide nanoparticles. Nano Mater. Sci. *1*, 48–59. https://doi.org/10.1016/j.jmat.2018.12.005.

38. Wu, P., Kong, X., Feng, Y., Ding, W., Sheng, Z., Liu, Q., and Ji, G. (2023). Phase engineering on amorphous/crystalline γ-Fe_2O_3 nanosheets for boosting dielectric loss and high-performance microwave absorption. Adv. Funct. Mater. *34*, 2311983. https://doi.org/10.1002/adfm.202311983.

39. Jia, Z., Liu, J., Gao, Z., Zhang, C., and Wu, G. (2024). Molecular intercalation-induced two-phase evolution engineering of 1T and 2H-MS_2 (M=Mo, V, W) for interface-polarization-enhanced electromagnetic absorbers. Adv. Funct. Mater. 2405523. https://doi.org/10.1002/adfm.202405523.

40. Zhang, D., Zhang, H., Cheng, J., Raza, H., Liu, T., Liu, B., Ba, X., Zheng, G., Chen, G., and Cao, M. (2020). Customizing coaxial stacking VS_2 nanosheets for dual-band microwave absorption with superior performance in the C- and Ku-bands. J. Mater. Chem. C *8*, 5923–5933. https://doi.org/10.1039/d0tc00763c.

41. Zhang, W., Zhang, X., Wu, H., Yan, H., and Qi, S. (2018). Impact of morphology and dielectric property on the microwave absorbing performance of MoS_2-based materials. J. Alloys Compd. *751*, 34–42. https://doi.org/10.1016/j.jallcom.2018.04.111.

42. Wu, F., Xia, Y., Sun, M., and Xie, A. (2018). Two-dimensional (2D) few-layers WS_2 nanosheets: An ideal nanomaterials with tunable electromagnetic absorption performance. Appl. Phys. Lett. *113*, 052906. https://doi.org/10.1063/1.5040274.

43. Du, B., Liu, Y., Xu, J., Ouyang, Y., Cheng, Y., and Zhang, T. (2023). Fabrication and electromagnetic wave absorbing properties of the $(Hf_{0.25}Zr_{0.25}Nb_{0.25}Ta_{0.25})C$ high-entropy ceramics. J. Alloys Compd. *969*, 172403. https://doi.org/10.1016/j.jallcom.2023.172403.

44. Zhang, J., Zhan, Y., Ren, Z., Wang, W., Zhang, Z., Zhang, Q., Han, G., and Zhang, W. (2024). Synthesis of (WZrNbTaM)C (M=Cr, Ni, Ti) ceramic powders and the electromagnetic wave absorption in 2-18 GHz. J. Am. Ceram. Soc. *107*, 3313–3328. https://doi.org/10.1111/jace.19642.

45. Ma, Y., Pan, A., Yang, X., Yuan, H., Li, Y., Chen, J., and Zhang, S. (2024). Molten salt synthesis of highly crystalized (TaNbTiV)C flake and its electromagnetic wave absorption property. Ceram. Int. *50*, 81–93. https://doi.org/10.1016/j.ceramint.2023.09.347.

46. Wang, W., Sun, G., Sun, X., Zhang, Z., Zhang, J., Liang, Y., and Bi, J. (2023). Electromagnetic wave absorbing properties of high-entropy transition metal carbides powders. Mater. Res. Bull. *163*, 112212. https://doi.org/10.1016/j.materresbull.2023.112212.

47. Ma, Y., Zhang, S., Yang, X., Wang, Q., Li, Y., Chen, J., and Zhang, S. (2023). Preparation and electromagnetic absorption properties of bulk (MgCoNiCuZn)O. J. Electron. Mater. *52*, 6959–6967. https://doi.org/10.1007/s11664-023-10619-z.

48. Zhang, W., Zhao, B., Xiang, H., Dai, F.Z., Wu, S., and Zhou, Y. (2021). One-step synthesis and electromagnetic absorption properties of high entropy rare earth hexaborides (HE REB_6) and high entropy rare earth hexaborides/borates (HE REB_6/HE $REBO_3$) composite powders. J. Adv. Ceram. *10*, 62–77. https://doi.org/10.1007/s40145-020-0417-2.

49. Zhang, W., Dai, F.Z., Xiang, H., Zhao, B., Wang, X., Ni, N., Karre, R., Wu, S., and Zhou, Y. (2021). Enabling highly efficient and broadband electromagnetic wave absorption by tuning impedance match in high-entropy transition metal diborides (HE TMB_2). J. Adv. Ceram. *10*, 1299–1316. https://doi.org/10.1007/s40145-021-0505-y.

50. Liu, C., Chen, Q., Li, X., Xiong, Z., Han, J., Yang, G., Yang, K., Wang, Y., Cheng, Y., and Jiang, N. (2024). Low-temperature synthesis of novel diboride ceramic with electromagnetic wave absorption properties. J. Mater. Sci. Mater. Electron. *35*, 287. https://doi.org/10.1007/s10854-024-12044-2.

51. Hui, S., Zhou, X., Zhang, L., and Wu, H. (2024). Constructing multiphase-induced interfacial polarization to surpass defect-induced polarization in multielement sulfide absorbers. Adv. Sci. *11*, 2307649. https://doi.org/10.1002/advs.202307649.

52. Zhao, B., Yan, Z., Li, D., Zhou, X., Du, Y., Wu, Y., Yang, L., Zhang, J., Zhang, D.W., and Che, R. (2023). Hierarchical flower-like sulfides with increased entropy for electromagnetic wave absorption. ACS Appl. Mater. Interfaces *15*, 59618–59629. https://doi.org/10.1021/acsami.3c15017.

53. Luo, W., Jiang, X., Liu, Y., Yuan, X., Huo, J., Li, P., and Guo, S. (2024). Entropy-driven morphology regulation of MAX phase solid solutions with enhanced microwave absorption and thermal insulation performance. Small *20*, 2305453. https://doi.org/10.1002/smll.202305453.

54. Xu, T., Li, J., Zhao, D., Chen, X., Sun, G., and Zhou, Z. (2023). Structural Engineering Enabled Bimetallic $(Ti_{1-y}Nb_y)_2AlC$ Solid Solution Structure for Efficient Electromagnetic Wave Absorption in Gigahertz. Small *19*, 2300119. https://doi.org/10.1002/smll.202300119.

55. Chen, C., Xi, J., Zhou, E., Peng, L., Chen, Z., and Gao, C. (2018). Porous graphene microflowers for high-performance microwave absorption. Nano-Micro Lett. *10*, 26. https://doi.org/10.1007/s40820-017-0179-8.

56. Zhang, H., Luo, N., Liu, T., Chen, F., and Fu, Q. (2022). Light-weight, low-loading and large-sheet reduced graphene oxide for high-efficiency microwave absorber. Carbon *196*, 1024–1034. https://doi.org/10.1016/j.carbon.2022.05.062.

57. Xu, W., Li, S., Wu, Y., Zhang, W., Yu, W., Zhou, Y., Fan, S., Bei, G., Ding, S.A., and Ding, S. (2022). Two-dimensional nanosheets of titanium carbonitride Ti_3CNT_x MXene for microwave absorption in the X and Ku bands. ACS Appl. Nano Mater. *5*, 17133–17141. https://doi.org/10.1021/acsanm.2c04062.

58. Qiao, L., Bi, J., Liang, G., Yang, Y., Wang, H., and Wang, S. (2023). Synthesis of high-entropy MXenes with high-efficiency electromagnetic wave absorption. J. Adv. Ceram. *12*, 1902–1918. https://doi.org/10.26599/JAC.2023.9220796.

59. Zhang, J., Xue, W., and Chen, X.Y. (2020). $Ti_3C_2T_x$ MXenes as thin broadband absorbers. Nanotechnology *31*, 275301. https://doi.org/10.1088/1361-6528/ab80fd.

60. He, H., Mir, I.A., Miao, B., Wang, S., Zhao, Y., Wang, M., and Bai, J. (2025). Synthesis of $(TiyVzCr1\text{-}y\text{-}z)_3C_2T_x$ MXene for excellent electromagnetic wave absorption properties. J. Alloys Compd. *1010*, 177521. https://doi.org/10.1016/j.jallcom.2024.177521.

61. Qing, Y., Zhou, W., Luo, F., and Zhu, D. (2016). Titanium carbide (MXene) nanosheets as promising microwave absorbers. Ceram. Int. *42*, 16412–16416. https://doi.org/10.1016/j.ceramint.2016.07.150.

62. Sha, Y., Zheng, J., Liu, K., Du, H., Watanabe, K., Taniguchi, T., Jia, J., Shi, Z., Zhong, R., and Chen, G. (2024). Observation of a Chern insulator in crystalline ABCA-tetralayer graphene with spin-orbit coupling. Science *384*, 414–419. https://doi.org/10.1126/science.adj8272.

Please cite this article in press as: Gu et al., Lattice distortion boosted exceptional electromagnetic wave absorption in high-entropy diborides, Matter (2025), https://doi.org/10.1016/j.matt.2025.102004

63. Zhang, Y., Yu, R., and Zhu, J. (2022). Displacement separation analysis from atomic-resolution images. Ultramicroscopy *232*, 113404. https://doi.org/10.1016/j.ultramic.2021.113404.

64. Wang, W., Liu, S., Wang, Y., Jia, B., Huang, Y., Xie, L., Jiang, B., and He, J. (2024). Tailoring local chemical fluctuation of high-entropy structures in thermoelectric materials. Sci. Adv. *10*, eadp4372. https://doi.org/10.1126/sciadv.adp4372.

65. Ding, Q., Zhang, Y., Chen, X., Fu, X., Chen, D., Chen, S., Gu, L., Wei, F., Bei, H., Gao, Y., et al. (2019). Tuning element distribution, structure and properties by composition in high-entropy alloys. Nature *574*, 223–227. https://doi.org/10.1038/s41586-019-1617-1.

66. Cowley, J.M. (1950). An approximate theory of order in alloys. Physiol. Rev. *77*, 669–675. https://doi.org/10.1103/physrev.77.669.

67. Wen, Z., Tang, Z., Meng, H., Zhuang, L., Yu, H., and Chu, Y. (2024). Ultrafast synthesis of high-entropy carbides up to 3,273 K for superior oxidation resistance. Cell Rep. Phys. Sci. *5*, 101821. https://doi.org/10.1016/j.xcrp.2024.101821.

68. Ophus, C., Ciston, J., and Nelson, C.T. (2016). Correcting nonlinear drift distortion of scanning probe and scanning transmission electron microscopies from image pairs with orthogonal scan directions. Ultramicroscopy *162*, 1–9. https://doi.org/10.1016/j.ultramic.2015.12.002.

69. Zhang, Q., Zhang, L.Y., Jin, C.H., Wang, Y.M., and Lin, F. (2019). CalAtom: A software for quantitatively analysing atomic columns in a transmission electron microscope image. Ultramicroscopy *202*, 114–120. https://doi.org/10.1016/j.ultramic.2019.04.007.

70. Blöchl, P. (1994). Projector augmented-wave method. Phys. Rev. B *5*, 17953–17979. https://doi.org/10.1103/physrevb.50.17953.

71. Kresse, G., and Furthmüller, J. (1996). Efficiency of ab-initio total energy calculations for metals and semiconductors using a plane-wave basis set. Comput. Mater. Sci. *6*, 15–50. https://doi.org/10.1016/0927-0256(96)00008-0.

72. Perdew, J., Burke, K., and Ernzerhof, M. (1996). Generalized gradient approximation made simple. Phys. Rev. Lett. *77*, 3865–3868. https://doi.org/10.1103/physrevlett.77.3865.

73. Zunger, A., Wei, S., Ferreira, L., and Bernard, J. (1990). Special quasirandom structures. Phys. Rev. Lett. *65*, 353–356. https://doi.org/10.1103/PhysRevLett.65.353.

74. van de Walle, A. (2009). Multicomponent multisublattice alloys, nonconfigurational entropy and other additions to the alloy theoretic automated toolkit. Calphad *33*, 266–278. https://doi.org/10.1016/j.calphad.2008.12.005.

75. Monkhorst, H., and Pack, J. (1976). Special points for Brillouin-zone integrations. Phys. Rev. B *13*, 5188–5192. https://doi.org/10.1103/PhysRevB.16.1748.

76. Lee, C., Song, G., Gao, M.C., Feng, R., Chen, P., Brechtl, J., Chen, Y., An, K., Guo, W., Poplawsky, J.D., et al. (2018). Lattice distortion in a strong and ductile refractory high-entropy alloy. Acta Mater. *160*, 158–172. https://doi.org/10.1016/j.actamat.2018.08.053.

77. Freysoldt, C., Grabowski, B., Hickel, T., Neugebauer, J., Kresse, G., Janotti, A., and Van de Walle, C.G. (2014). First-principles calculations for point defects in solids. Rev. Mod. Phys. *86*, 253–305. https://doi.org/10.1103/revmodphys.86.253.

78. Chu, H., Li, R., Feng, P., Wang, D., Li, C., Yu, Y., and Yang, M. (2024). First-principles calculations for point defects in solids. ACS Catal. *14*, 1553–1566. https://doi.org/10.1103/revmodphys.86.253.